Soft Template-Based Synthesis of Mesoporous Phosphorus- and Boron-Codoped NiFe-Based Alloys for Efficient Oxygen Evolution Reaction

Yunqing Kang, Yanna Guo, Jingjing Zhao, Bo Jiang, Jingru Guo, Yi Tang, Hexing Li, Victor Malgras, Mohammed Amin, Hiroki Nara, et al.

Soft-Templating Synthesis of Mesoporous Phosphorus- and Boron-Doped NiFe-Based Alloy Architectures for Efficient Oxygen Evolution Reaction

Yunqing Kang,[1,2] Yanna Guo,[3] Jingjing Zhao,[4] Bo Jiang,[4] Jingru Guo,[2] Yi Tang,[2] Hexing Li,[4] Victor Malgras,[2,5] Hiroki Nara,[3] Yoshiyuki Sugahara,[3,6,7] Yusuke Yamauchi*[2,3,8] and Toru Asahi*[1,3,7]

1 Department of Life Science and Medical Bioscience, School of Advanced Science and Engineering, Waseda University, 3-4-1 Okubo, Shinjuku, Tokyo 169-8555, Japan

2 JST-ERATO Yamauchi Materials Space-Tectonics Project and International Center for Materials Nanoarchitectonics (WPI-MANA), National Institute for Materials Science (NIMS), 1-1 Namiki, Tsukuba, Ibaraki 305-0044, Japan

3 JST-ERATO Yamauchi Materials Space-Tectonics Project, Kagami Memorial Research Institute for Materials Science and Technology, Waseda University, 2-8-26 Nishiwaseda, Shinjuku, Tokyo 169-0051, Japan

4 The Education Ministry Key Lab of Resource Chemistry and Shanghai Key Laboratory of Rare Earth Functional Materials, Shanghai Normal University, Shanghai 200234, China

5 Aix Marseille Université, Université de Toulon, CNRS, IM2NP, UMR 7334, Campus de St. Jérôme, 13397 Marseille, France

6 Department of Applied Chemistry, School of Advanced Science and Engineering, Waseda University, 3-4-1 Okubo, Shinjuku, Tokyo 169-8555, Japan

7 Department of Nanoscience and Nanoengineering, School of Advanced Science and Engineering, Waseda University, 3-4-1 Okubo, Shinjuku, Tokyo 169-8555, Japan

8 Australian Institute for Bioengineering and Nanotechnology (AIBN) and School of Chemical Engineering, The University of Queensland, Brisbane, QLD 4072, Australia

Abstract

Controls of morphologies, compositions, and crystalline phases of mesoporous non-noble metal catalysts provide great opportunities to improve their performance. Herein, well-defined phosphorus (P)- and boron (B)-doped NiFe alloy mesoporous nanospheres (NiFeB-P MNs) with adjustable Ni/Fe ratio and large pore size (11 nm) are synthesized *via* the soft-templated chemical reduction strategy followed by a phosphine steam phosphidation process. Earth-abundant NiFe-based materials are considered as promising electrocatalysts for oxygen evolution reaction (OER) due to their low cost and high intrinsic catalytic activity. The resulting NiFeB-P MNs exhibit a low OER overpotential of 252 mV at 10 mA cm^{-2}, significantly smaller than that of B-doped NiFe mesoporous nanospheres (274 mV), and commercial RuO_2 (269 mV) in alkaline electrolyte. This work highlights the practicality of designing mesoporous architecture of non-noble metals and the importance of further incorporating P to adjust the electronic structure of the metal-B-based alloy and enhance the intrinsic activity of the catalyst.

Key words: *mesoporous metals; non-noble metals alloy; soft-templating synthesis; nonmetal-elements doping*

Introduction

Several strategies such as morphology control,[1,2] composition adjustment,[3-5] and phase engineering,[6,7] have been reported as effective ways to bring out new chemical and physical properties in energy materials. Mesoporous architectures have shown many merits including high surface areas, tunable pore structures and controllable chemical compositions.[8] Among them, conductive metallic mesoporous materials yield highly exposed active sites and efficient mass/electron transports in a wide range of electrochemical reactions.[9-11] In addition, the metallic mesoporous materials with large pore size are conducive to facilitate the smooth and fast mass transport for large reagent molecules.[12] The mesoporous structure in metals can be templated by the lyotropic liquid crystal (LLC) [13] or the hard-templating approaches.[14] Yet, the high viscosity of LLC is responsible for limiting the flexibility of this approach, while the hard-templating methods require multiple steps and harsh conditions to remove templates like silica[15] and always has limited pore size.[16] Unlike the above-mentioned methods, self-assembly of surfactant molecules into micelles provides a facile and versatile strategy for preparing a wide range of mesoporous materials with advantages such as controllable pore sizes and wall thicknesses.[17] Previously reported mesoporous metals and alloys prepared through micelle self-assembly and chemical reduction processes, however, have been mostly limited to crystalline noble metal-based materials.[18] Compared to noble metal (*e.g.*, Pt and Pd) ions, which can be easily reduced by moderate reducing agent such as ascorbic acid,[18] the chemical reduction of non-precious metal (*e.g.*, Ni, Co, Fe and Cu) ions is more difficult due to their low redox potential. This means that non-precious metals usually require stronger reducing agents such as sodium borohydride and/or dimethylamine borane, which cause drastic reduction process and release large amounts of H_2, making the mesoporous structure more difficult to construct. Therefore, more precisely controlling the chemical reduction conditions and expanding the micelle self-assembly approach to the synthesis of non-precious metals and their alloys are the next logical step to reach sustainable solutions.

The oxygen evolution reaction (OER) takes place at the anode, which collects electrons to facilitate the generation of oxygen gas from water. This reaction is the bottleneck for achieving efficient electrochemical water-splitting and rechargeable metal-air-batteries, and has thus attracted tremendous attention in the past decades.[19] The sluggish kinetics involving the four electron-proton coupled reaction prevent these systems from being of practical use, and hence the development of highly efficient OER electrocatalysts is desired.[20] The state-of-the-art

electrocatalysts for water oxidation use noble metal-based materials such as RuO_2 and IrO_2; however, they rely on scarce elements which severely hinder their widespread application.[21] Instead, enormous efforts have been devoted to exploit non-noble transition metal-based materials. In particular, NiFe-based catalysts have been demonstrated as one of the most efficient OER catalysts in alkaline electrolytes and have attracted tremendous attention over the past years.[22,23] The incorporation of Fe in the Ni site improves substantially the reaction rate while lowering the overpotential.[24] The rational design of NiFe-based materials therefore is extremely promising for enhancing electrochemical OER performance.

NiFe-based compounds have been generally prepared in the form of nanoparticles,[25,26] core-shell structures,[27] and hollow spheres.[28] Although well-known NiFe layered double hydroxides (LDH) possess a high OER performance, the nanosheet structures are disadvantaged by their tendency to aggregate, their limited active edge sites, and their poor conductivity.[29] To the best of our knowledge, there are very few studies devoted to the synthesis of NiFe-based materials with well-defined large mesoporous nanospheres. Unlike Ni- or Co-based ions,[30,31] dissolved Fe species can easily form hydroxides[32] and the Fe species also tend to form unstable green rust $Fe^{II}_{x}Fe^{III}_{y}(O,OH,Cl)_{z}$, which can be further oxidated to $Fe^{III}OOH$.[33] These reasons make the deposition of Fe ions more complicated and difficult.

Apart from nanomorphology control, it has been previously reported that introducing metalloids or nonmetals (*e.g.*, B, N, S or P) in Ni-based catalysts can facilitate charge transfer, adjust the balance of adsorbed/desorbed OER intermediates, and alter the electronic structure of the electrocatalysts, thereby enhancing the conversion efficiency.[34-37] In the case of metal-boron-based materials synthesized using chemical reduction approach, the introduction of B into the non-noble metals (*eg.*, Ni, Co, Fe) usually suppresses crystallization and obtains an amorphous structure,[38] which has abundant defects and active sites, resulting in enhancement in OER performance.[39] Compared to single element incorporation, the co-existence of two or more these nonmetals/metalloids elements may further influence the catalytic properties of metal-based active sites. For example, incorporating P into the metal-B-based species have been demonstrated to effectively boost the OER catalytic activity due to fact that P enables additional adjustment of the electronic structure of the metals and enhancement in electrical conductively, as well as decrease the energy barrier of the OER path by promoting the adsorption for oxygen-containing

intermediates.[40-43] It is therefore expected that incorporating P in mesoporous NiFeB-based nanomaterials is a promising way to further boost the OER catalytic performance.

Motivated by the aforementioned promising tactics, in this study we design and synthesize a catalyst from mesoporous P- and B-doped NiFe alloy (abbreviated as 'NiFeB-P') with open large pore size (11 nm) to fabricate an electrocatalyst for OER. Amorphous NiFeB mesoporous nanospheres (MNs) with turntable Ni/Fe ratio and adjustable pore size are first synthesized by a soft-templated chemical reduction method in the presence of polymeric micelles. Then, the typical NiFeB-P MNs are successfully obtained by a two-stage phosphine steam phosphidation process at moderate temperature (*i.e.,* 220 °C). This gentle technique can introduce metal phosphides in the pore walls of the electrocatalysts while ensuring the approximate integrity of the mesoporous structure. The obtained NiFeB-P MNs exhibit excellent electrocatalytic activity and stability toward the OER in alkaline media.

Result and discussion

Figure 1a shows the schematic representation of the synthesis of NiFeB MNs and following typical P-doped NiFeB-P MNs. Firstly, the NiFeB MNs were synthesized by a self-assembly of micelles using dimethylamine borane (DMAB) as the main reducing agent. The formation of micelles in the mixed solvents (*i.e.*, DMF + aqueous solution) can be confirmed by the Tyndall effect and transmission electron microscope (TEM) observations (**Figure S1**). The reaction solution is initiated by a small amount of sodium borohydride (SBH) solution under argon protection. Since a the initially SBH generated amorphous NiFeB nuclei can continually catalyze the decomposition of DMAB, this self-catalytic process lasts for one hour to complete the final NiFeB MNs deposition. After drying, an oxide layer is detected by X-ray photoelectron spectroscopy (XPS) on the obtained NiFeB MNs, as can be expected from simple air exposure (**Figure S2**). Next, PH_3 released from the thermal decomposition of NaH_2PO_2 ($2NaH_2PO_2 \rightarrow PH_3\uparrow + Na_2HPO_4$) was used to react with the oxidized surface of the NiFeB MNs at 220 °C to form NiFeB-P MNs (**Figure S3**).[44]

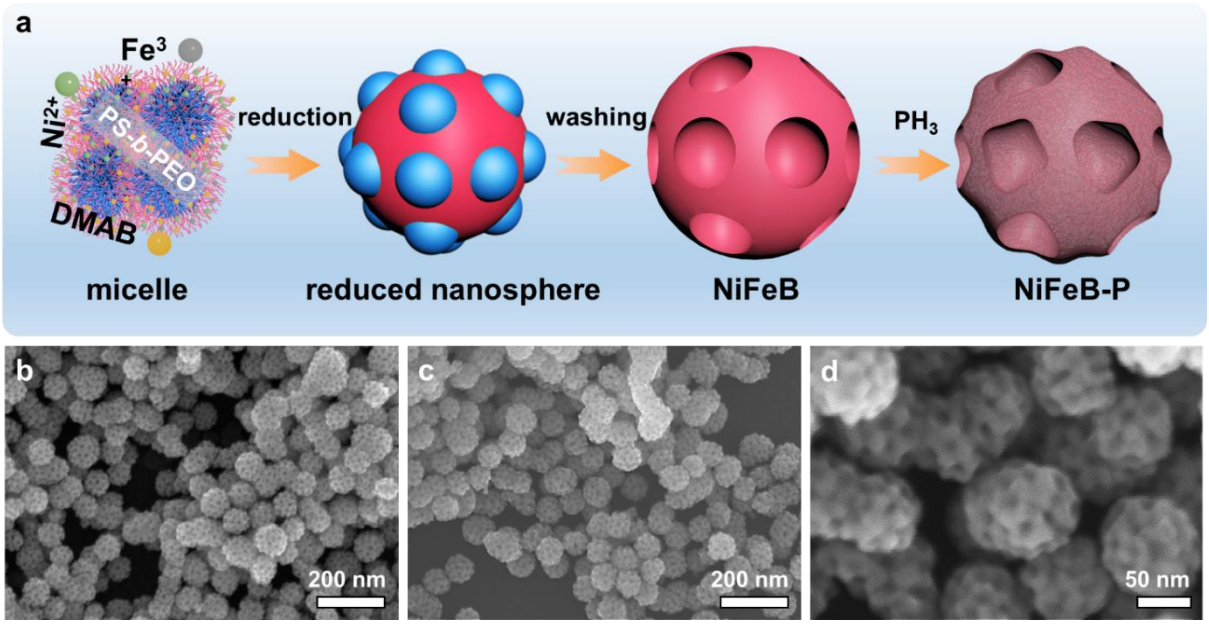

Figure 1. a) Schematic illustration describing the preparation of NiFeB-P MNs. b) SEM image of the prepared NiFeB MNs. c-d) low- and high-resolution SEM images of NiFeB-P MNs.

Scanning electron microscope (SEM) and transmission electron microscope (TEM) images reveal that the well-dispersed NiFeB MNs have a large number of mesopores well-distributed over the outer surface (**Figure 1b** and **Figure S4**). After phosphidation reaction, the NiFeB-P MNs also retain a porous morphology, although this step results in slight shrinkage of the particles (**Figure**

1c-d). The average particle size and mesopore size of the NiFeB-P MNs are measured to be 82 and 11 nm, respectively (**Figure S5**). From the TEM observations (**Figure 2a**), the well-distributed mesopores and uniform morphology of the NiFeB-P can be clearly observed. The Ni:Fe:B:P atomic ratio is determined by inductively coupled plasma optical emission spectroscopy (ICP-OES) to be 63 : 9 : 19 : 9 (**Table S1**).

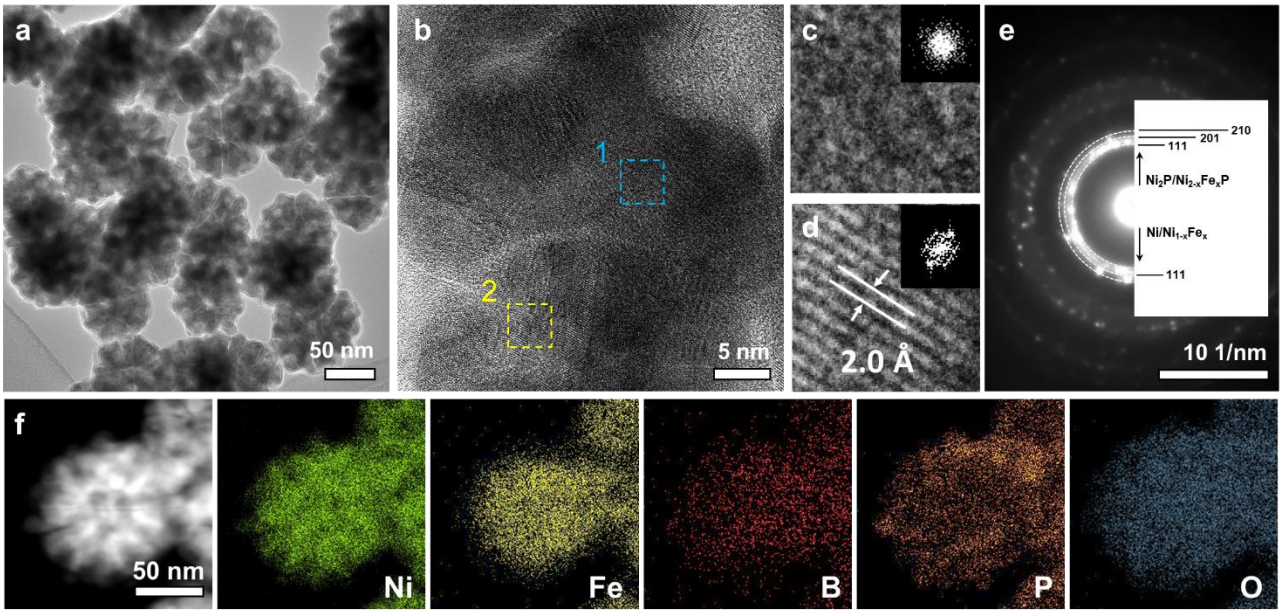

Figure 2. a) TEM and b) HRTEM images of NiFeB-P MNs. c, d) Enlarged HRTEM images and corresponding FFT patterns of the selected area "1" and "2" in b), respectively. e) SAED pattern of NiFeB-P MNs. f) HAADF-STEM and elemental mapping images of NiFeB-P MNs.

The successful doping of P in NiFeB-P MNs can be clearly investigated by high-resolution TEM (HRTEM) observation. As shown in **Figure 2b**, amorphous and crystalline domains coexist in the NiFeB-P MNs, and their representative area are marked in region "1" and "2", respectively, further enlarged in **Figure 2c** and **d**. The corresponding selected-area fast Fourier transform (FFT) patterns show a diffuse ring (inset **Figure 2c**) and the bright spots (inset **Figure 2d**). The amorphous region is mainly derived from as-synthesized NiFeB. The well-resolved lattice fringe with a *d*-spacing of 2.0 Å in **Figure 2d** is likely to correspond to the (201) plane of *hcp* Ni_2P/Fe_2P and/or the (111) plane of *fcc* NiFe.[45] The selected-area electron diffraction (SAED) pattern (**Figure 2e**) also shows the polycrystalline feature of NiFeB-P MNs. The phosphidation process at 220 °C results in the presence of semi-crystallization structure while retaining part of the amorphous feature. In contrast, the NiFeB MNs appear to be completely amorphous as no clear lattice fringes can be observed by

HRTEM (**Figure S6**). The high-angle annular dark-field scanning TEM (HAADF-STEM) image and the corresponding element mapping images show the homogeneous distribution of Ni, Fe, B, P and O elements in the NiFeB-P MNs (**Figure 2f**).

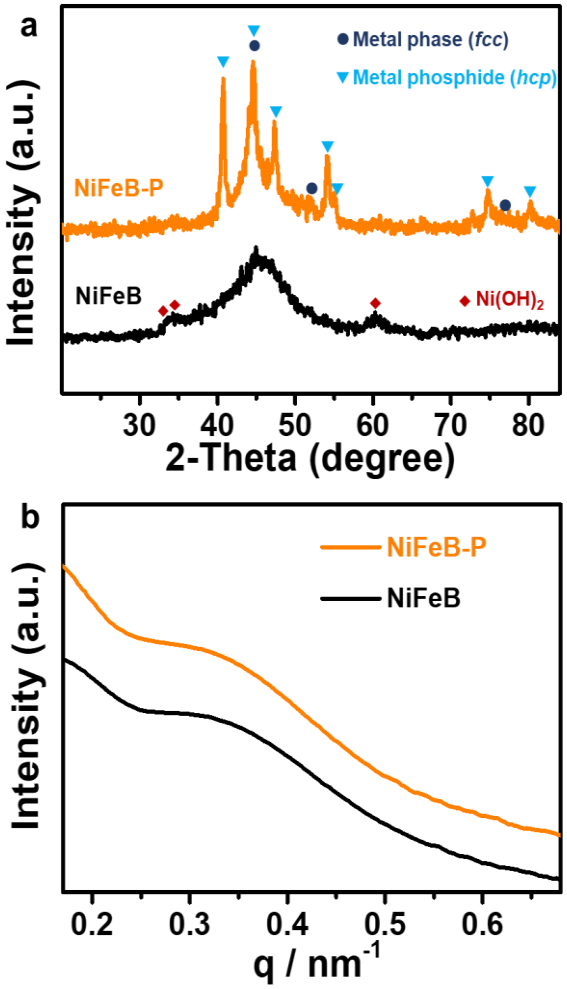

Figure 3. a) XRD and b) SAXS patterns of NiFeB and NiFeB-P MNs.

The wide-angle X-ray diffraction (XRD) patterns of NiFeB and NiFeB-P MNs are shown in **Figure 3a**, in which one broad peak is observed at $2\theta = 45°$ for the NiFeB MNs, usually observed for amorphous materials.[37] During the chemical reduction process using DMAB as reducing agent, the small sized boron, generated from the decomposition of DMAB, can dope into the lattice of NiFe, resulting an amorphous nature of NiFeB MNs (**Figure 3a**). The amorphous structure has a large number of adsorption and active sites, which make it unique and attractive for efficient electrocatalysis of water splitting.[39,46] Due to the oxidation of the surface in the air, traces of $Ni(OH)_2$ (JCPDS No. 22-0444) can be also observed in NiFeB MNs before phosphidation, however the intensity and width of the peak suggest the presence of scarce nanocrystallites. After

phosphidation at 220 °C, the presence of NiFe alloy (*fcc*) and Ni_2P (JCPDS No. 89-4864)/Fe_2P (JCPDS No. 51-0943) (*hcp*) can be observed. Based on the ICP result (**Table S1**), the resulting NiFeB-P MNs have a large amount of Ni content. Although the lattice parameters of Ni_2P and Fe_2P are close to make it difficult to distinguish in our experiment,[47] Ni_2P is more stable and easier to form due to their different formation enthalpies (−161 and −131 kJ mol^{-1}, respectively).[48] This reason may lead to the main component of Ni_2P species in NiFeB-P MNs. As a controlled experiment, the sample donated as NiFeB-220 MNs were also prepared at 220 °C omitting the phosphorus source ($NaH_2PO_2 \cdot H_2O$). Instead of metal phosphides diffraction peaks, semi-crystallized NiFe alloy becomes the dominant phase (**Figure S7**). After thermal treatment at 220 °C, the broad peak observed for NiFeB becomes shaper. The XRD peaks at 2θ = 44.5° in both NiFeB-P and NiFeB-220 MNs correspond to the (111) plane of *fcc* Ni (JCPDS No. 04-0850) without an obvious shift (It should be noted that, according to the detailed discussion about the effect of phosphidation temperatures on the crystallinity and crystalline phases, we notice a very slight shift of the main peak after incorporating Fe atoms into the *fcc* and/or *hcp* crystal, which will be explained later.). Small-angle X-ray scattering (SAXS) patterns provide evidence of the pore-to-pore distance uniformity in both the NiFeB-P and NiFeB MNs (**Figure 3b**), estimated as 18.7 nm, according to the peak centered at q = 0.34 nm^{-1}.

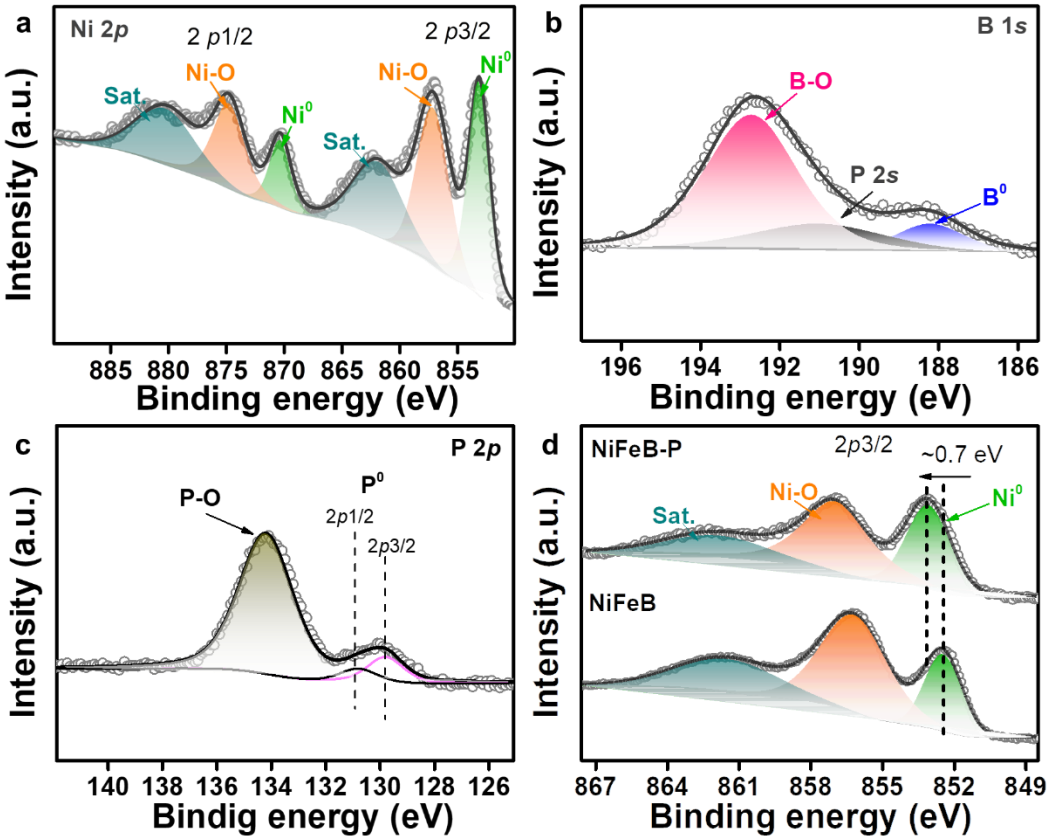

Figure 4. XPS spectra of a) Ni 2*p*, b) B 1*s*, and c) P 2*p* of NiFeB-P MNs. d) Compared XPS spectra on Ni 2*p*3/2 of NiFeB-P and NiFeB MNs.

XPS was used to evaluate the element valence states on the surface of the NiFeB-P MNs. The survey scan reveals the co-existence of Ni, Fe, B, P and O elements on the sample surface (**Figure S8a**). The existence of Fe can be confirmed from the weak Fe 3*p* peak (**Figure S8b**),[49] however, the valuable information from the Fe 2*p* peak cannot be extracted due to a substantial overlap with the Ni LMM Auger peaks under an Al electron source.[50,51] The high-resolution Ni 2*p* doublet at binding energy (BE) of 853.1 and 870.3 eV can be assigned to metallic nickel (Ni^0), confirming the form of metal borides; while the oxidized Ni (Ni-O) doublet is located at 857.0 and 874.7 eV (**Figure 4a**).[1] In **Figure 4b**, the B 1*s* signal in NiFeB-P can be deconvoluted into peaks located at 188.2 and 192.7 eV, assigned to B-metal (B^0) and oxidized B (B-O) species, respectively (as well as a weak and broad P 2*s* contribution). In comparison with the pure B (187.1 eV),[52] the BE of boron in NiFeB-P is positively shift of 1.1 eV, indicating the electronic interaction between B and NiFe (*i.e.*, the electron transfer from B to metals). The O 1*s* spectra (**Figure S8c**) in NiFeB-P MNs is composed of the O1 (531.9 eV) and O2 (532.8 eV) peaks, which are assigned to lattice oxygen and chemisorbed oxygen species/water molecules, respectively.[43] Both metal-P (P^0) and oxidized P

peaks are also detected (**Figure 4c**). Notably, compared to NiFeB MNs, the BEs of Ni 2*p* in NiFeB-P MNs is positively shift ~0.7 eV, which indicates that the electrons transfer from Ni to P (**Figure 4d**). This characteristic of P accepting electrons from metal atoms has been often reported in past literatures.[42,53,54]

The soft-templating method based on the self-assembly of micelles allow the facile controllable the pore size of mesoporous materials. For example, SEM images in **Figure S9 a-d** show the resulted NiFeB MNs (after removing the soft-templates) prepared using different kind of PS-*b*-PEO diblock copolymers (*i.e.*, PS_{1600}-*b*-PEO_{2900}, PS_{3000}-*b*-PEO_{2600}, PS_{5000}-*b*-PEO_{2200}, and PS_{9500}-*b*-PEO_{5000}.) with different molecular weights of PS chains. The size of mesopores distinctly expanded from 5 to 18 nm by increasing the molecular weights of PS chains (**Figure S9e**). Theses result demonstrate that the hydrophobic PS groups in PS-*b*-PEO micelles greatly influences the final size of mesopores. In addition to the controllable pore size, the Ni/Fe composition of NiFeB catalysts can be adjusted by changing the feeding ratio of metal precursors (**Figure S10a-e**). However, when the Ni^{2+}:Fe^{3+} feeding ratio reaches 80:20, merging polydisperse mesoporous nanospheres are produced (**Figure S11**). This is due to the high content of Fe^{3+} species tend to form hydroxides in the reaction solution (**Figure S11b**), which probably negatively impact the dispersion of the metal nanospheres as well as on the porous morphology (**Figure S11c,d**). The well-defined mesopores and monodisperse samples are expected to enhance the exposure of active site and mass transportation. Therefore, we studied the electrochemical activity of samples with Fe feeding content increasing from 0 to 15%, which possess similar well-defined mesoporous structure. The OER activity increases with the higher proportion of Fe and the catalyst with a feeding Ni:Fe atomic ratio of 85:15 gives the highest current density (**Figure S10f**). Thus, the amorphous NiFeB alloy MNs catalyst (**Table S1**) prepared with a feeding Ni:Fe atomic ratio of 85:15 was selected to study the effect of phosphidation on its OER activity.

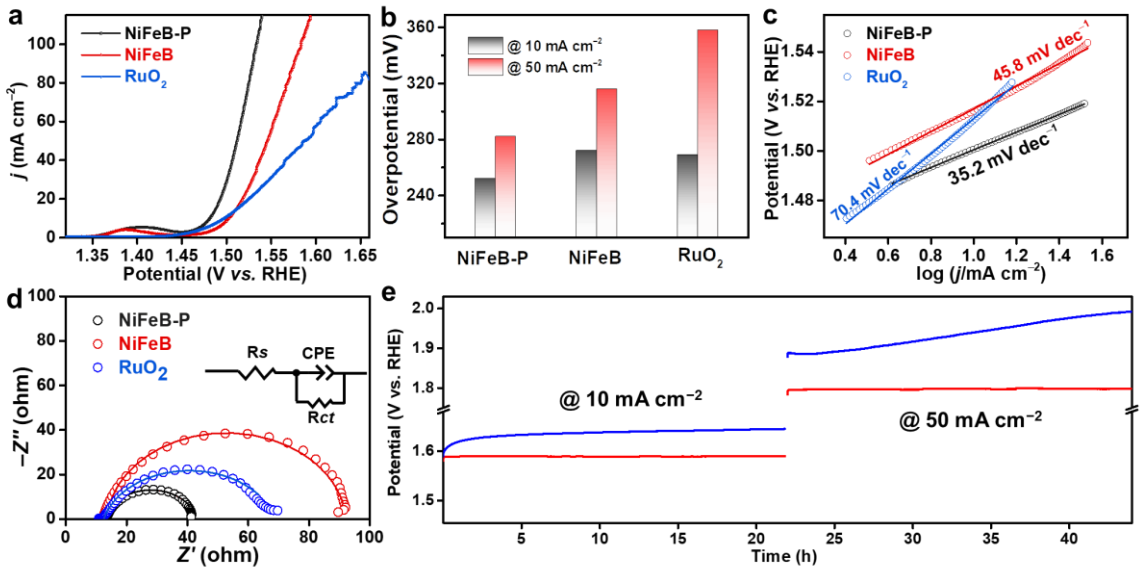

Figure 5. Electrocatalytic oxygen evolution reaction. a) LSV curves of NiFeB-P, NiFeB MNs and commercial RuO_2 electrodes for OER in 1 M KOH solution at scan rate of 10 mV s^{-1} corrected by *iR* compensation. b) Comparison of overpotentials at 10 and 50 mA cm^{-2}. c) The corresponding Tafel plots of the samples. d) EIS analyses Nyquist plots (the inset shows the equivalent circuit model) of different electrodes recorded performed at 1.5 V *vs.* RHE. e) Chronopotentiometry measurements of NiFeB-P MNs and RuO_2 at a constant current density of 10 and 50 mA cm^{-2} for a long-term stability test.

The electrochemical performance toward OER was measured in a typical three electrode cell in 1 M KOH electrolyte and normalized by the geometric surface area with a selected scan rate of 10 mV s^{-1} (**Figure S12**). **Figure 5a** compares the OER polarization curves of the different catalysts with commercial RuO_2. Among them, NiFeB-P MNs displays a smaller overpotential of 252 and 283 mV at a current density of 10 (η_{10}) and 50 (η_{50}) mA cm^{-2}, respectively, compared to NiFeB MNs before phosphidation (η_{10} = 272 mV, η_{50} = 316 mV) and commercial RuO_2 (η_{10} = 269 mV, η_{50} = 358 mV) (**Figure 5b**). The Tafel plots derived from the LSV curves are known to reflect the OER kinetics of all catalysts. As presented in **Figure 5c**, the NiFeB-P MNs exhibit the smallest Tafel slope of 35.2 mV dec^{-1} as compared to NiFeB MNs (45.8 mV dec^{-1}) and commercial RuO_2 (70.4 mV dec^{-1}), indicating faster oxygen evolution kinetics. From electrochemical impedance spectroscopy (EIS) tests, the charge transfer resistance (*R*ct) of NiFeB-P MNs is found to be only 28.7 Ω at potential of 1.5 V *vs.* RHE, smaller than NiFeB (78.6 Ω) and RuO_2 (57.9 Ω), which indicates a faster charge transfer kinetics between the electrode surface and the electrolyte during the OER process (**Figure 5d**).

To better understand the mechanism of the enhanced OER performance in NiFeB-P MNs, the electrochemical double-layer capacitances (C_{dl}) of the catalysts in the non-Faradic potential window were calculated to estimate the electrochemical surface areas (ECSA).[55] The cyclic voltammetry (CV) curves of the as-prepared samples were measured to evaluate the C_{dl} at different scan rates from 20 to 100 mV s^{-1} (**Figure S13a,b**). The superior C_{dl} (0.70 mF cm^{-2}) in NiFeB-P MNs suggests a larger ECSA and more exposed electrochemical active sites towards OER (**Figure S13c**). In addition, we compared the ECSA-normalized activity in **Figure S13d**, which shows that NiFeB-P MNs have higher activity than NiFeB MNs. These results show that the superior high OER activity in NiFeB-P MNs is due not only to increasing electrochemical active surface area, but also to the higher intrinsic activity. Previously reported density functional theory (DFT) study determined that the coexistence of B and P can shift the *d*-band center of Ni and Fe upwards toward the Fermi energy level and enhance *p*-*d* hybridization. The narrower *d*-band center would be beneficial to strengthen interactions among chemically active sites, thereby improving the OER activity.[41] The NiFeB-P MNs catalyst also shows superior OER performance to most reported non-noble-metal-based electrocatalysts loaded on glassy carbon electrode (**Table S2**). Although the overpotential of NiFeB-P MNs is lower than the catalysts such as Co-Fe-B-P (η_{10} = 225 mV)[56] and LiCoBPO ((η_{10} = 245 mV),[57] which supported on conductive porous nickel foam, the mass loading (0.09 mg cm^{-2}) in our catalyst is much lower than them (*e.g.*, 0.46 and 3 mg cm^{-2} for Co-Fe-B-P and LiCoBPO, respectively).

The separated two-stage temperature control system can take advantage of a temperature differential. Specifically, maintaining the temperature T_I of the tube furnace I (**Figure S3**) at 300 °C ensures that PH_3 is properly released from the $NaH_2PO_2 \cdot H_2O$ powders. Different crystallinities and phosphide contents were obtained by adjusting the temperature T_{II} (*i.e.*, 180, 220, 260, 350 °C) of the second tube furnace II containing the NiFeB MNs. All these samples show a certain level of mesostructural ordering, according to the SEM images in **Figure S14a-d**. Excess crystallization beyond 220 °C detected by XRD (**Figure S14e**) seems to compromise the mesoporosity. The results show that up to 220 °C, the dominant phase is metal phosphides (as previously stated, it is expected that the Ni_2P is preferably formed over Fe_2P). Beyond 260 °C, the NiFe alloy phase is predominantly observed, with a minor content of metal phosphides, although the (111) reflection of metal *fcc* crystal phase overlaps the (201) reflection of metal phosphide *hcp* crystal. The atomic radius of Fe is slightly larger than that of Ni, which explains why the lattice of Ni *fcc* crystal is

shifted after substitution with Fe (**Figure S14f**).[50] With increasing phosphidation temperature, it is expected that a larger number of Fe atoms may be incorporated into the Ni *fcc* crystal structure and/or *hcp* Ni_2P crystal structure. There are obvious shifts observed in the XRD patterns and no other peaks derived from impurities. The increasing phosphidation temperature is expected to promote the transition from amorphous to crystalline phase, along with an increase in average crystallite sizes, judging from the full width at half maximum, FWHM, for each peak. From the electrochemical behavior towards OER (**Figure S14g**), the sample treated at 220 °C shows the highest activity, thus demonstrating that the electrocatalytic performance of NiFeB MNs can be modulated through phosphidation process at 220 °C.

The OER activity of nonporous NiFeB-P nanospheres, synthesized without PS-*b*-PEO porogens, was also scrutinized to highlight the effect of mesoporosity (**Figure S15**). The Brunauer–Emmett–Teller (BET) surface area is significantly lower in the nonporous catalyst (4.7 *vs*. 26.8 $m^2\ g^{-1}$), obtained from N_2 adsorption–desorption isotherm (**Figure S15b**). The NiFeB-P has a uniformly sized mesopores centered at around 10 nm, obtained from the pore size distribution curve based on Barrett-Joyner-Halenda analysis (inset **Figure S15b**), similar to the SEM result (**Figure S5**). The reduced active area and limited mass/charge transports in nonporous NiFeB-P are likely the reason for the inferior OER performance (**Figure S15c**).

For better understand the effect of P on the OER performance, we also synthesized reference sample NiFeB-220 MNs, which is thermal treated of NiFeB MNs at 220 °C in N_2 atmosphere without PH_3 steam. SEM image in **Figure S16a** shows the NiFeB-220 MNs still possess a well-defined mesoporous structure. However, the increased overpotential in NiFeB-220 MNs highlights the importance of metal phosphides in NiFeB-P MNs (**Figure S16b**). The obvious oxidation peak prior to OER observed in NiFeB-P and NiFeB-220 MNs samples (**Figure 5a**) results from the transition from Ni^{2+} to Ni^{3+} and/or Ni^{4+}.[58] We found that the Ni redox waves shift toward higher potential in NiFeB-P MNs, which confirming the change in the electronic structure by phosphidation. In addition, EIS results indicate that NiFeB-P MNs have a much rapid charge transfer kinetics than NiFeB-220 (**Figure S16c**). Overall, further incorporating of P results a more favourable electronic configuration and promoted electrical conductivity, thus showing a high intrinsic OER activity.

During alkaline OER, metal borides/phosphides are oxidized to their corresponding metal oxide or (oxy)hydroxides,[19] which usually act as the real active phases. Recently, Dionigi et al.[59]

demonstrated that synergy between the Ni and Fe sites at the formed redox phases can stabilize OER intermediates by forming the O-bridged NiFe reaction center, resulting a low overpotential for OER. In our case, we also observe surface reconfiguration in the NiFeB-P MNs (supported on carbon black), in which the NiFe oxide/oxyhydroxides layer are gradually formed after several CV cycling, as confirmed by SEM results (**Figure S17**). The *in-situ* transformation process has not a big influence on the internal porous structure, which will be discussed later. Furthermore, as seen in **Figure S18**, the NiFeB-P MNs also exhibit a lower overpotential than the NiFeB-P@NiFe LDH (the NiFe LDH was *ex-situ* formed on the surface of NiFeB-P MNs), probably due to the high conductively of metallic NiFeB-P MNs.

Another important criterion to assess the electrocatalytic performance is the long-term stability. LSV polarization curves show that the NiFeB-P MNs have a slight degradation after continuous CV cycling, which is significant superior to RuO_2 (**Figure S19**). After hundreds of CV cycles, chronopotentiometry tests were conducted on the NiFeB-P and RuO_2 catalysts, at a constant current density of 10 and 50 mA cm^{-2} in 1 M KOH. As shown in **Figure 5e**, the NiFeB-P MNs can operate stalely over 44 h, superior to the commercial RuO_2 catalyst.

TEM and XPS analysis were performed after OER stability test to further investigate structural and chemical change in the NiFeB-P MNs catalyst. The spherical mesoporous morphology is mostly retained after long-term OER test (**Figure S20a**). However, TEM (**Figure S20b**) and HRTEM (**Figure S20c**) images reveal the formation of an amorphous layer on the surface of the particles, matching the SEM results (**Figure S17**). It is known that NiFe-based alloys and oxides are prone to form amorphous NiFe oxide/oxyhydroxides under alkaline conditions, which are a class of high-performance OER catalysts.[29,37] The presence of open pores provides ideal sites for the growth of such active amorphous layer. HAADF-STEM-EDS analysis (**Figure S20d**) shows that Ni, Fe, B, P and O are still homogeneously distributed over the mesoporous nanospheres. Furthermore, in the XPS spectrum of Ni 2*p* (**Figure S21a**), the Ni^0 peaks have almost disappeared, leaving the NiO_x species only. Since the amount of Fe content is very low (9.1 at.% from ICP) and the Ni LMM Auger peak overlaps to the Fe 2*p* peak under an Al electron source, it is rather difficult to discuss the assignment of Fe 2*p* peak. However, the positive shift observed for the main peak of Fe 3*p* (**Figure S21b**) suggests to appearance of oxidated species.[60] P^0 and B^0 can no more be observed, and only very weak peaks attributed to their oxidated states appear on the spectra (**Figure S21c-d**). The results indicate that the metal borides/phosphides undergo the surface reconstruction and form

real active amorphous oxide/oxyhydroxides phases,[41,61] as also confirmed by XRD results (**Figure S22**). This *in-situ* formed metal oxide/oxyhydroxide layer has been considered to be protecting the inner layer from being further corroded, leading to a good stability.[42] Although surface B and P might be dissolved or transferred during OER, it is reported that such feature can help bring more lattice vacancies, increasing the utilization of metal active sites.[43] The small amounts of residual nonmetals (B and P) is reported to promote electron transfer or moderate bonding to the OER intermediates.[62] Overall, the NiFeB-P during OER process can retain both the mesoporous architecture and the surface enriched with amorphous metal oxides/oxyhydroxides, which are major performance factors in heterostructured electrocatalysts. An electrolytic water splitting device can be realized by using NiFeB-P MNs as OER catalyst and commercial 20 *wt.*% Pt/C as HER catalyst (**Figure S23a**). The gas volume ratio close to 2:1 can be observed in H_2 and O_2, which has a faradaic efficiency of 98.2% and 98.0%, respectively (**Figure S23b,c**). Considering the fact that incorporating high-valence transition-metal modulators, such as W, Mo and Ta etc., can decrease the OER overpotential by the readier oxidation transition of Ni, Co, Fe-based metals,[63] it is desirable to further explore the effect of these high-valence modulators on OER performance in the field of well-defined mesoporous architectures. In addition, accelerating the application of these catalysts in industrially field is also highly desired.[64]

Conclusion

The well-defined mesoporous P- and B-doped NiFe alloy nanospheres (NiFeB-P MNs) with large mesopores have been prepared using a block copolymer self-assembly method followed by a phosphidation process. During the chemical reduction process, B plays a crucial role in generating a large number of defects in the amorphous structure, which facilitates the provision of more active sites. The moderate phosphidation process allows for further P doping while maintaining the basic integrity of the mesopore morphology and preserving part of the amorphous structure. The obtained electrocatalysts exhibits better OER performance in alkaline media, superior to that of commercial RuO_2 benchmark. The activity of samples without phosphidation mostly relies on the high surface area and good mass transfer originating from the mesoporous structure, which provides ideal sites for *in-situ* formation of highly active NiFe oxides/oxyhydroxides layer during water oxidation process. The addition of P in the system provides an efficient way to further tune the electronic structures of active sites and enhance the electrical conductivity, yielding a substantial increase in

the intrinsic activity. This work provides a strategy to design high-performance water splitting electrocatalysts and investigating the influence of composition- and morphology-dependent properties on their performance. Further enhancing the OER performance by incorporating other high-valence metals and accelerating the development in industrialization are still desirable in the future work.

Experimental section

Synthesis of NiFeB MNs. The amorphous NiFeB alloy mesoporous nanoparticles, denoted as NiFeB MNs, were synthesized according to a wet chemical reduction process. Typically, the first mixture was prepared by dissolving 10 mg of PS-*b*-PEO block copolymer in 3.0 mL of DMF resulting in a transparent solution. Then, 3.0 mL of water was added. The metal precursor was prepared by adding of 3.4 mL of 60 mM $Ni(OCOCH_3)_2 \cdot 4H_2O$, 0.6 mL of 60 mM $FeCl_3 \cdot 6H_2O$, and 6.0 mL of 0.5 M dimethylamineborane (DMAB) mixed with 0.3 g Bu_4PBr powder in a vial. The utilization of Bu_4PBr can not only reduce the formation of soap bubbles (resulted from the H_2 produced by the decomposition of DMAB in the micellar system) by increasing the surface tension of the solution, but also moderate the reduction rate by decreasing the reducibility of metal species.[11] After dissolution of the Bu_4PBr, the metal precursor solution was then added to the above block copolymer mixture. The resulting mixed solution was moved to a two-neck flask and kept at 40 ^oC in oil bath and purged with argon for 3.0 minutes to remove oxygen from the solution to prevent metal oxidation during the reaction. Then pre-cooled 100 μL 2.0 mg/mL of a sodium borohydride (SBH) solution was added into the above solution, allowing to stand for 1.0 hour to complete the NiFeB deposition. Finally, the product was collected by centrifugation and washed with mixed solution of acetone and ethanol several times to remove the template, and then it was dried at room environment. The final molar ratio of Ni and Fe in the products was adjusted by using different precursor ratios. For comparison, nonporous NiFeB was prepared in the same procedures without using block copolymer. In this work, the pore sizes of NiFeB MNs were varied by changing the diblock copolymers (PS-*b*-PEO) with different the molecular weights of PS blocks, including PS_{1600}-*b*-PEO_{2900}, PS_{3000}-*b*-PEO_{2600}, PS_{5000}-*b*-PEO_{2200}, and PS_{9500}-*b*-PEO_{5000}.

Synthesis of NiFeB-P MNs. The NiFeB-P MNs were synthesized by a controlled steam cooling phosphidation method in two connected tube furnaces. Briefly, $NaH_2PO_2 \cdot H_2O$ acted as the phosphine source were loaded in a boat, and then placed at the first tube furnace (T_1). The dried

NiFeB MNs in the other boat were placed at the second tube furnace (T_{II}) downstream of the steam sources. Keep the mass ratio of $NaH_2PO_2 \cdot H_2O$ to NiFeB MNs at 25:1. Then, the Part I and Part II (shown in **Figure S3**) were concurrently heated up to 300 and 220 °C, respectively, with a ramp rate of 2 °C min^{-1} under N_2 flow (blowing from T_I to T_{II}). After 1 h, the product was collected for characterization. The different crystallinity and phosphidation samples could be obtained by adjusting the different temperature (*i.e.*, 180, 220, 260, 350 °C) at the Part II at same time keeping with the temperature of the Part I at 300 °C. For comparison, the NiFeB MNs without P doping (NiFeB-220) were prepared at one tube furnace by annealing the NiFeB MNs at 220 °C under N_2 protection omitting the $NaH_2PO_2 \cdot H_2O$. The nonporous NiFeB-P catalyst was synthesized by the same procedure except by using nonporous NiFeB nanoparticles instead of NiFeB MNs.

Characterization. X-ray Diffraction (XRD) was conducted on a Smart lab X-ray diffractometer (RIGAKU) at a scanning rate of 5 deg min^{-1} with a Cu Kα radiation (40 kV, 30 mA) source. Scanning electron microscopy (SEM) images were obtained on a Hitachi SU-8000 with an operating voltage of 10 kV. Transmission electron microscope (TEM) and high-resolution transmission electron microscopy (HRTEM) observations were performed on a JEOL JEM-3010 operated at 300 kV and equipped with an energy-dispersive spectrometer. For TEM observation, the sample was diluted in ethanol solution and sonicated for 10 min. The 2-3 drops (~20 uL) were deposited on a standard lacey carbon grid (ultra-high-resolution carbon film UHR-C10). X-ray photoelectron spectroscopy (XPS) was carried by PHI Quantera SXM (ULVAC-PHI) using an Al monochromatic Kα X-ray source. Small-angle X-ray scattering measurements (SAXS; Rigaku NANO-Viewer) were used to evaluate the porous structure of the samples. The atomic compositions of the samples were characterized with inductively coupled plasma optical emission spectroscopy (ICP-OES; Hitachi model SPS3520UV-DD). For details, 1 mg of sample was weighed and transferred into Zr crucible. Then, 0.5 g of Na_2CO_3 and 0.5 g of Na_2O_2 were added into the crucible and then the crucible was heated to fuse the sample with flux. After cooling, Milli-Q water, and 10 mL of HCl (1+1) were added into the crucible to dissolve melt. This solution was poured into 50 mL volumetric flask and the 2 mL of 100 mg/L Y standard solution was added. The solution was diluted to marked line with Milli-Q water, used for ICP-OES. Nitrogen adsorption-desorption isotherms were got from a BELSORP-mini (BEL, Japan) at 77 K. The pore size distributions of NiFeB-P MNs was calculated based on the Barrett-Joyner-Halenda (BJH) model.

Electrochemical Measurements. All electrochemical measurements were carried out in three-electrode cell using electrochemical workstation (CHI 660EZ) at room temperature. Glassy carbon electrode (GCE) with diameter of 3 mm coated with catalysts was used as working electrode. The saturated calomel electrode (SCE) and graphite rod were used as reference electrode and counter electrode, respectively. Since pure mesoporous metal nanospheres tend to agglomerate during phosphidation and are poorly dispersed on GCE, we use carbon black (Vulcan XC–72) as the support (without OER activity) to distribute metal catalysts and ensure uniform dispersion of catalysts on the GCE. Specifically, the carbon black-supported catalyst was prepared using 10 mg of carbon black mixed with the as-synthesized samples (loading amount of 44.0 *wt*.% according to ICP-OES) and then dispersed in 20 mL ethanol solution. After sonicated for 1 h to ensure the formation of well-dispersed suspension, the above mixture was washed three times by ethanol and subsequently dried at room temperature. Then, the obtained powders were in the final phosphidation reaction at a controllable temperature under N_2/PH_3 steam for 1 h. Electrocatalyst inks were prepared by dispersing 5 mg of carbon-supported samples into a solution containing mixture, 980 μL of ethanol and 20 μL of Nafion solution (5 *wt*.%), followed by ultrasonication for 1 h. Before the electrochemical test, GCE was carefully polished and washed with water obtain a clean surface. Subsequently, 3 μL of the catalyst ink were dropped onto the polished GCE (mass loading of NiFeB-P MNs: 0.09 mg cm^{-2}) and evaporated to dry at room temperature. Before the OER measurement, continuous CV around 20 cycles at a scan rate of 100 mV s^{-1} from 1.2 to 1.6 V *vs.* RHE was conducted to result stable electrocatalysts. Linear sweep voltammetry (LSV) was conducted at a scan rate of 10 mV s^{-1} in 1 M KOH solution. Tafel plots were derived from the overpotential versus the log (current density) according to the corresponding LSV curves and the Tafel slope was calculated with the following equation: $\eta = a + b \log j$, where η was the overpotential, a was the exchange current density, b was the Tafel slope, and j was the current density. The applied potentials were calibrated against RHE, $E_{RHE} = E_{SCE} + 1.054$ (in 1 M KOH) (calibration curve is shown in **Figure S24**), and all the polarization curves were ohmic potential drop (*iR*) corrected. To compare the apparent electrochemical double-layer capacitance (C_{dl}), cyclic voltammetry (CV) curves were performed in non-Faradaic region. The C_{dl} was estimated by plotting the at $\Delta J = (J_a - J_C)/2$ at 1.11V versus RHE against the scan rate. Assuming that the specific capacitance for a flat surface is 40 μF cm^{-2} per cm^2_{ECSA}, the ECSA is calculated from the fowling equation: ECSA= $C_{dl} \div 0.04 \times S$ (cm^2_{ECSA}), where S is the surface area of the electrode.[65]

Electrochemical impedance spectroscopy (EIS) was performed over a frequency range of 0.1–100 kHz. For long-term stability test, the same loading amounts (1 mg cm^{-2}) of catalysts were loaded on the carbon fiber paper and cycled CV hundred times at a scan rate of 100 mV S^{-1} in 1 M KOH to form the stable catalysts. Then the stability tests were performed using chronopotentiometry at a constant current density of 10 and 50 mA cm^{-2}. Considering the long operation OER in strong alkaline solution causes instability of SCE electrode, which affects stability results, a more stable reference electrode of Hg/HgO electrode (0.92 V *vs*. RHE, in 1 M KOH) was used instead of SCE when we conducted the long-term stability measurements.

A small water splitting device is februated by using NiFeB-P MNs as OER catalyst and commercial 20% Pt/C as HER catalyst. The catalysts were loaded on carbon fiber paper (1 mg cm^{-2}) substrate due to its high conductivity, quickly releasing the produced gas, and allowing for large amounts of catalysts. The produced H_2 and O_2 are confirmed by gas chromatography (GC, Shimadzu Tracera, BID-2010) and are separately measured by a water displacement method in a gastight (**Figure S23**). By comparing the experimental value with the theoretical calculation value, the Faradaic efficiencies were investigated for both OER and HER. The plot was converted into mmol *vs.* time format using the Faraday's law of electrolysis: $n = Q/ZF$, where n is the number of moles, Q is the charge passed during electrolysis, F is Faraday's constant (96 485 C mol^{-1}), and Z = 2 and 4 is the number of electrons involved of HER and OER, respectively.

Author contributions

Yunqing Kang: Investigation, Visualization, Formal analysis, Writing-original draft. Yanna Guo: Investigation, Formal analysis. Bo Jiang: Conceptualization, Investigation. Jingru Guo: Investigation. Yi Tang: Formal analysis. Hexing Li: Supervision, Investigation. Victor Malgras: Formal analysis, Writing-Review & Editing. Hiroki Nara: Formal analysis. Yoshiyuki Sugahara: Investigation. Yusuke Yamauchi: Supervision, Resources, Writing-Review & Editing, Project administration. Toru Asahi: Supervision, Validation, Visualization, Project administration.

Acknowledgements

This work was supported by the China Scholarship Council (CSC). This work was jointly supported by the JST-ERATO Yamauchi Materials Space-Tectonics Project (JPMJER2003) and the Australian National Fabrication Facility (Queensland Node).

References

[1] Y. Guo, J. Tang, Z. Wang, Y. Sugahara, Y. Yamauchi, *Small* **2018**, 14, 1802442.
[2] X. Teng, J. Wang, L. Ji, Y. Lv, Z. Chen, *Nanoscale* **2018**, 10, 9276.
[3] Q. Xu, H. Jiang, X. Duan, Z. Jiang, Y. Hu, S. W. Boettcher, W. Zhang, S. Guo, C. Li, *Nano Letters* **2021**, 21, 492.
[4] M. Khalid, A. M. B. Honorato, G. Tremiliosi Filho, H. Varela, *J. Mater. Chem. A* **2020**, 8, 9021.
[5] G. Liu, M. Wang, Y. Wu, N. Li, F. Zhao, Q. Zhao, J. Li, *Appl. Catal. B* **2020**, 260, 118199.
[6] G. Chen, Y. Zhu, H. M. Chen, Z. Hu, S.-F. Hung, N. Ma, J. Dai, H.-J. Lin, C.-T. Chen, W. Zhou, Z. Shao, *Adv. Mater.* **2019**, 31, 1900883.
[7] Y. Wang, Y. Zhou, M. Han, Y. Xi, H. You, X. Hao, Z. Li, J. Zhou, D. Song, D. Wang, F. Gao, *Small* **2019**, 15, 1805435.
[8] Y. Yan, G. Chen, P. She, G. Zhong, W. Yan, B. Y. Guan, Y. Yamauchi, *Adv. Mater.* **2020**, 32, 2004654.
[9] J. Wei, Z. Sun, W. Luo, Y. Li, A. A. Elzatahry, A. M. Al-Enizi, Y. Deng, D. Zhao, *J. Am. Chem. Soc* **2017**, 139, 1706.
[10] O.-H. Kim, Y.-H. Cho, S. H. Kang, H.-Y. Park, M. Kim, J. W. Lim, D. Y. Chung, M. J. Lee, H. Choe, Y.-E. Sung, *Nat. Commun.* **2013**, 4, 2473.
[11] Y. Kang, B. Jiang, J. Yang, Z. Wan, J. Na, Q. Li, H. Li, J. Henzie, Y. Sakka, Y. Yamauchi, T. Asahi, *ACS Nano* **2020**, 14, 17224.
[12] Y. Deng, J. Wei, Z. Sun, D. Zhao, Chem. *Soc. Rev.* **2013**, 42, 4054.
[13] Y. Yamauchi, A. Sugiyama, R. Morimoto, A. Takai, K. Kuroda, *Angew. Chem., Int. Ed.* **2008**, 47, 5371.
[14] H. Lv, D. Xu, C. Kong, Z. Liang, H. Zheng, Z. Huang, B. Liu, *ACS Cent. Sci.* **2020**, 6, 2347.
[15] H. Wang, H. Y. Jeong, M. Imura, L. Wang, L. Radhakrishnan, N. Fujita, T. Castle, O. Terasaki, Y. Yamauchi, *J. Am. Chem. Soc.* **2011**, 133, 14526.
[16] Y. Shi, Y. Wan, D. Zhao, *Chem. Soc. Rev.* **2011**, 40, 3854.
[17] C. Li, Q. Li, Y. V. Kaneti, D. Hou, Y. Yamauchi, Y. Mai, *Chem. Soc. Rev.* **2020**, 49, 4681.
[18] V. Malgras, H. Ataee-Esfahani, H. Wang, B. Jiang, C. Li, K. C. W. Wu, J. H. Kim, Y. Yamauchi, *Adv. Mater.* **2016**, 28, 993.
[19] N.-T. Suen, S.-F. Hung, Q. Quan, N. Zhang, Y.-J. Xu, H. M. Chen, *Chem. Soc. Rev.* **2017**, 46, 337.
[20] Y. Hao, Y. Li, J. Wu, L. Meng, J. Wang, C. Jia, T. Liu, X. Yang, Z.-P. Liu, M. Gong, *J. Am. Chem. Soc.* **2021**, 143, 1493.
[21] K. Zeng, X. Zheng, C. Li, J. Yan, J.-H. Tian, C. Jin, P. Strasser, R. Yang, *Adv. Funct. Mater.* **2020**, 30, 2000503.
[22] M. Gong, H. Dai, *Nano Res.* **2015**, 8, 23.
[23] J. Mohammed-Ibrahim, *J. Power Sources* **2020**, 448, 227375.
[24] K. Zhu, X. Zhu, W. Yang, *Angew. Chem., Int. Ed.* **2019**, 58, 1252.

[25] L. Du, L. Luo, Z. Feng, M. Engelhard, X. Xie, B. Han, J. Sun, J. Zhang, G. Yin, C. Wang, Y. Wang, Y. Shao, *Nano Energy* **2017**, 39, 245.
[26] J. M. V. Nsanzimana, Y. Peng, Y. Y. Xu, L. Thia, C. Wang, B. Y. Xia, X. Wang, *Adv. Energy Mater.* **2018**, 8, 1701475.
[27] L. Yu, H. Zhou, J. Sun, F. Qin, F. Yu, J. Bao, Y. Yu, S. Chen, Z. Ren, *Energy Environ. Sci.* **2017**, 10, 1820.
[28] C. Zhang, M. Shao, L. Zhou, Z. Li, K. Xiao, M. Wei, *ACS Appl. Mater. Interfaces* **2016**, 8, 33697.
[29] J. Zhao, J.-J. Zhang, Z.-Y. Li, X.-H. Bu, *Small* **2020**, 16, 2003916.
[30] Y. Kang, J. Henzie, H. Gu, J. Na, A. Fatehmulla, B. S. A. Shamsan, A. M. Aldhafiri, W. A. Farooq, Y. Bando, T. Asahi, B. Jiang, H. Li, Y. Yamauchi, *Small* **2020**, 16, 1906707.
[31] B. Jiang, H. Song, Y. Kang, S. Wang, Q. Wang, X. Zhou, K. Kani, Y. Guo, J. Ye, H. Li, Y. Sakka, J. Henzie, Y. Yusuke, *Chem. Sci.* **2020**, 11, 791.
[32] A. Stefánsson, *Environ. Sci. Technol.* **2007**, 41, 6117.
[33] Y. Yamauchi, M. Komatsu, M. Fuziwara, Y. Nemoto, K. Sato, T. Yokoshima, H. Sukegawa, K. Inomata, K. Kuroda, *Angew. Chem., Int. Ed.* **2009**, 48, 7792.
[34] J. Masa, W. Schuhmann, *ChemCatChem* **2019**, 11, 5842.
[35] Y. Li, H. Zhang, M. Jiang, Q. Zhang, P. He, X. Sun, *Adv. Funct. Mater.* **2017**, 27, 1702513.
[36] Q. Zhang, T. Li, J. Liang, N. Wang, X. Kong, J. Wang, H. Qian, Y. Zhou, F. Liu, C. Wei, Y. Zhao, X. Zhang, *J. Mater. Chem. A* **2018**, 6, 7509.
[37] G. Liu, D. He, R. Yao, Y. Zhao, J. Li, *Nano Res.* **2018**, 11, 1664.
[38] Y. Pei, G. Zhou, N. Luan, B. Zong, M. Qiao, F. Tao, *Chem. Soc. Rev.* **2012**, 41, 8140.
[39] S. Anantharaj, S. Noda, *Small* **2020**, 16, 1905779.
[40] H. Ren, X. Sun, C. Du, J. Zhao, D. Liu, W. Fang, S. Kumar, R. Chua, S. Meng, P. Kidkhunthod, L. Song, S. Li, S. Madhavi, Q. Yan, *ACS Nano* **2019**, 13, 12969.
[41] F. Hu, H. Wang, Y. Zhang, X. Shen, G. Zhang, Y. Pan, J. T. Miller, K. Wang, S. Zhu, X. Yang, C. Wang, X. Wu, Y. Xiong, Z. Peng, *Small* **2019**, 15, 1901020.
[42] W. Tang, X. Liu, Y. Li, Y. Pu, Y. Lu, Z. Song, Q. Wang, R. Yu, J. Shui, *Nano Res.* **2020**, 13, 447.
[43] J. Kwon, H. Han, S. Jo, S. Choi, K. Y. Chung, G. Ali, K. Park, U. Paik, T. Song, *Adv. Energy Mater.* **2021**, 11, 2100624.
[44] Q. Guan, W. Li, *J. Catal.* **2010**, 271, 413.
[45] M. Wang, M. Lin, J. Li, L. Huang, Z. Zhuang, C. Lin, L. Zhou, L. Mai, *Chem. Commun.* **2017**, 53, 8372.
[46] H. Liang, A. N. Gandi, C. Xia, M. N. Hedhili, D. H. Anjum, U. Schwingenschlögl, H. N. Alshareef, *ACS Energy Letters* **2017**, 2, 1035.
[47] A. Cho, J. Shin, A. Takagaki, R. Kikuchi, S. T. Oyama, *Top. Catal.* **2012**, 55, 969.
[48] M. E. Schlesinger, *Chem. Rev.* **2002**, 102, 4267.
[49] T. Yamashita, P. Hayes, *Appl. Surf. Sci.* **2008**, 254, 2441.
[50] M. Chen, S. Lu, X.-Z. Fu, J.-L. Luo, *Adv. Sci.* **2020**, 7, 1903777.
[51] J. Chen, F. Zheng, S.-J. Zhang, A. Fisher, Y. Zhou, Z. Wang, Y. Li, B.-B. Xu, J.-T. Li, S.-G. Sun, *ACS Catal.* **2018**, 8, 11342.
[52] H. Li, H. Li, W.-L. Dai, W. Wang, Z. Fang, J.-F. Deng, *Appl. Surf. Sci.* **1999**, 152, 25.
[53] C.-C. Hou, Q. Li, C.-J. Wang, C.-Y. Peng, Q.-Q. Chen, H.-F. Ye, W.-F. Fu, C.-M. Che, N. López, Y. Chen, *Energy Environ. Sci.* **2017**, 10, 1770.
[54] W. Wang, P. Liu, K. Wu, K. Zhang, L. Li, Z. Qiao, Y. Yang, *New J. Chem.* **2015**, 39, 813.

[55] S. Anantharaj, S. R. Ede, K. Karthick, S. Sam Sankar, K. Sangeetha, P. E. Karthik, S. Kundu, *Energy Environ. Sci.* **2018**, 11, 744.
[56] Z. Wu, D. Nie, M. Song, T. Jiao, G. Fu, X. Liu, *Nanoscale* **2019**, 11, 7506.
[57] P. W. Menezes, A. Indra, I. Zaharieva, C. Walter, S. Loos, S. Hoffmann, R. Schlögl, H. Dau, M. Driess, *Energy Environ. Sci.* **2019**, 12, 988.
[58] L. Trotochaud, S. L. Young, J. K. Ranney, S. W. Boettcher, *J. Am. Chem. Soc.* **2014**, 136, 6744.
[59] F. Dionigi, Z. Zeng, I. Sinev, T. Merzdorf, S. Deshpande, M. B. Lopez, S. Kunze, I. Zegkinoglou, H. Sarodnik, D. Fan, A. Bergmann, J. Drnec, J. F. d. Araujo, M. Gliech, D. Teschner, J. Zhu, W.-X. Li, J. Greeley, B. R. Cuenya, P. Strasser, *Nat. Commun.* **2020**, 11, 2522.
[60] P. Mills, J. L. Sullivan, *J. Phys. D: Appl. Phys.* **1983**, 16, 723.
[61] P. F. Liu, X. Li, S. Yang, M. Y. Zu, P. Liu, B. Zhang, L. R. Zheng, H. Zhao, H. G. Yang, *ACS Energy Letters* **2017**, 2, 2257.
[62] F. Hu, S. Zhu, S. Chen, Y. Li, L. Ma, T. Wu, Y. Zhang, C. Wang, C. Liu, X. Yang, L. Song, X. Yang, Y. Xiong, *Adv. Mater.* **2017**, 29, 1606570.
[63] B. Zhang, L. Wang, Z. Cao, S. M. Kozlov, F. P. García de Arquer, C. T. Dinh, J. Li, Z. Wang, X. Zheng, L. Zhang, Y. Wen, O. Voznyy, R. Comin, P. De Luna, T. Regier, W. Bi, E. E. Alp, C.-W. Pao, L. Zheng, Y. Hu, Y. Ji, Y. Li, Y. Zhang, L. Cavallo, H. Peng, E. H. Sargent, *Nat. Catal.* **2020**, 3, 985.
[64] D. Siegmund, S. Metz, V. Peinecke, T. E. Warner, C. Cremers, A. Grevé, T. Smolinka, D. Segets, U.-P. Apfel, *JACS Au* **2021**, 1, 527.
[65] C. C. L. McCrory, S. Jung, J. C. Peters, T. F. Jaramillo, *J. Am. Chem. Soc.* **2013**, 135, 16977.